JOURNAL OF GEOPHYSICAL RESEARCH: OCEANS, VOL. 118, 7036–7048, doi:10.1002/2013JC008842, 2013

Intrusion of warm surface water beneath the McMurdo Ice Shelf, Antarctica

A. A. Stern,[1] M. S. Dinniman,[2] V. Zagorodnov,[3] S. W. Tyler,[4] and D. M. Holland[1]

Received 7 February 2013; revised 2 October 2013; accepted 29 October 2013; published 19 December 2013.

[1] A 6 month temperature record collected below McMurdo Ice Shelf in 2011–2012 shows the temporal and spatial structure of the summertime warm water signal that penetrates beneath the ice shelf. The strength and duration of the warm water intrusion suggest an annual melt rate at Windless Bight of 0.71 m/yr. A Ross Sea numerical model demonstrates a seasonal warm water pathway leading from the west side of the Ross Sea Polynya (RSP) toward McMurdo Sound. The warm water enters McMurdo Sound, subducts beneath the ice shelf and causes accelerated summer melting. Temperature data were recorded using Distributed Temperature Sensing fiber optics, which gives a vertical temperature profile at a 1 m vertical resolution. This study constitutes one of the first successful implementations of this technology in Polar Regions.

Citation: Stern, A. A., M. S. Dinniman, V. Zagorodnov, S. W. Tyler, and D. M. Holland (2013), Intrusion of warm surface water beneath the McMurdo Ice Shelf, Antarctica, *J. Geophys. Res. Oceans*, *118*, 7036–7048, doi:10.1002/2013JC008842.

1. Introduction

[2] The melting of the floating ice shelves around Antarctica is an important factor in determining the Antarctic Ice Sheet mass balance. Recent observations have shown that accelerating ice shelf melt rates are closely linked with increased ice velocities of the grounded ice flowing into those ice shelves [*Pritchard et al*., 2012; *Horgan et al*., 2011]. This results in an increase in the mass flux from the Antarctic continent into global oceans. However, due to the scarcity of data, the processes involved in ice shelf melting and the mechanisms delivering heat to the ice shelves are still uncertain. This uncertainty significantly reduces our ability to project sea-level rise in the coming century.

[3] Ice shelf melting processes and the intrusion of warm water beneath ice shelves can be described by three modes [*Jacobs et al*., 1992; *Hattermann et al*., 2012], as shown in the schematic in Figure 1 (M. Craven, personal communication, 2012). Mode 1 is the intrusion of High-Salinity Shelf Water (HSSW) into the ice shelf cavities along the seafloor bottom. HSSW is formed due to brine rejection from sea-ice formation. Since the HSSW is formed at the surface and the freezing point of salt water decreases with increased pressure, the HSSW is warmer than the freezing point at the grounding line and its intrusion causes melting at the grounding line [*MacAyeal*, 1984]. Mode 1 circulation causes melting in the grounding line areas of the Ross, Filchner-Ronne, and Amery Ice Shelves [*Jacobs et al*., 1992]. Mode 2 is the intrusion of Circumpolar Deep Water (CDW) into the ice shelf cavity at intermediate depths. The CDW can be more than 4°C warmer than the in situ freezing points and causes rapid melting. Mode 2 melting is largely responsible for the recent accelerated melt rates found on ice shelves by the Amundsen and Bellingshausen Seas [*Jacobs et al*., 2011]. Lastly, a mode 3 intrusion is caused by warm surface waters that enter the ice shelf cavity near the surface, forced by tides and/or seasonal currents, causing melting near the ice front [*Jacobs et al*., 1992].

[4] The three modes of circulation are not entirely distinct and can overlap and interact with one another. Interaction between the modes can be important for determining the heat and mass exchange beneath ice shelves [*Hattermann et al*., 2012]. Nevertheless, the modes provide a good framework for understanding ice shelf melting processes. The seasonal dependence of the different intrusion modes has been observed with satellites [*Horgan et al*., 2011; *Bindschadler et al*., 2011], moorings [*Nicholls*, 1996; *Makinson et al*., 2006], and in models [*Holland et al*., 2003; *Dinniman et al*., 2007, 2012], but is still not well understood. Here, we focus on mode 3 intrusions.

[5] Mode 3 intrusions are likely to be present to some extent on all of the Antarctic ice shelves and are responsible for 173 Gt/yr of ice shelf melt, which is a significant fraction of the total annual ice shelf attrition (544 Gt/yr) [*Jacobs et al*., 1992]. The melting due to mode 3 currents

Additional supporting information may be found in the online version of this article.

[1]Courant Institute of Mathematical Science, New York University, New York, New York, USA.
[2]Center for Coastal Physical Oceanography, Old Dominion University, Norfolk, Virginia, USA.
[3]Byrd Polar Research Center, Ohio State University, Columbus, Ohio, USA.
[4]Department of Geological Sciences and Engineering, University of Reno, Reno, Nevada, USA.

Corresponding author: A. A. Stern, Courant Institute of Mathematical Science, New York University, 212 Mercer St., New York, NY 10012, USA. (alon@cims.nyu.edu)

2169-9275/13/10.1002/2013JC008842

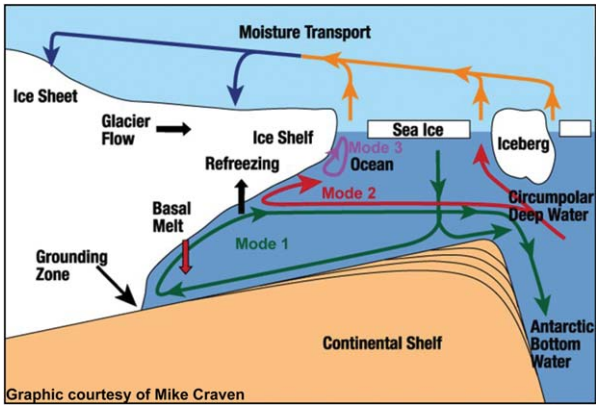

Figure 1. Schematic showing the three modes of warm water intrusion.

occurs within 100 km of the ice front, and leads to exponential thinning of the ice shelf toward the ice front [*Horgan et al*., 2011].

[6] As a step toward further understanding of mode 3 intrusions, results from measurements made beneath the McMurdo Ice Shelf at Windless Bight (WB) in 2011–2012 are presented. The McMurdo Ice Shelf was chosen for this study because the long history of measurements in McMurdo Sound means that we have a good understanding of the major current systems and oceanography in the region. Furthermore, recent measurements below the sea ice south of Ross Island [*Hunt et al*., 2003; *Mahoney et al*., 2011; *Robinson and Williams*, 2012] have shown that there is a warm water summer signal, which is a likely candidate for a regular mode 3 intrusion.

[7] A Ross Sea regional model is run to simulate the summer intrusion of warm water in McMurdo Sound. Model simulations are compared with observations made near the ice front and under the ice shelf. The observational data and the model data are both used to estimate the temperature impact of this warm water intrusion. The model results are also used to determine the source and timing of the warm water intrusion.

2. Background Oceanography

[8] Oceanographical observations since the 1980s indicate that the dominant current system in McMurdo Sound is a clockwise circulation [*Mitchell and Bye*, 1985; *Lewis and Perkin*, 1985; *Robinson et al*., 2010]. Warmer waters enter McMurdo Sound in the north-east from the Ross Sea, and run along the eastern boundary of McMurdo Sound (see Figure 2). Most of this water recirculates around the sound and leaves McMurdo Sound along the western boundary of the sound. Some of this water makes its way to the south-east, under the ice shelf. There is also a flow of water out from under the ice shelf in the west, which joins the main ocean current, exiting McMurdo Sound along the western boundary of the sound. The circulation is summarized in Figure 1a in *Robinson et al*. [2010].

[9] The water that moves under the ice shelf is directed by the bathymetry around Ross Island toward WB, following contours of constant ocean water column thickness [*Hunt et al*., 2003; *Mahoney et al*., 2011] (see Figure 2d). Water is able to pass under the ice shelf since the McMurdo Ice Front is only about 20 m thick. The ice thickness increases to 200 m over a distance of about 10 km [*Kovacs et al*., 1993]. The bottom ocean currents in the strait south of Ross Island are fairly consistent all year round since they are strongly controlled by the bathymetry [*MacAyeal*, 1984; *Robinson et al*., 2010], while higher up in the water column, the velocities show a seasonal variation [*Mahoney et al*., 2011]. In summer, a current in the upper half of the water column wraps around Cape Armitage (CA, Figure 2a) toward WB [*Mahoney et al*., 2011]. This current is responsible for the mode 3 intrusion and subsequent enhanced melting that occurs in the summer months.

[10] The two significant annual oceanographic signals that can be seen under the McMurdo Ice Shelf are the warm water summer signal, which enters through McMurdo Sound in December/January [*Hunt et al*., 2003; *Mahoney et al*., 2011; *Robinson and Williams*, 2012], and the arrival of ice shelf water in winter from under the Ross Ice Shelf [*Littlepage*, 1965; *Leonard et al*., 2006; *Mahoney et al*., 2011; *Robinson and Williams*, 2012]. This paper focuses on the summer warm water intrusion.

[11] Year-long temperature moorings have been deployed underneath the sea ice at the McMurdo Inlet Jetty (MIJ) and at CA in 1999, 2000 [*Hunt et al*., 2003], and 2008 [*Mahoney et al*., 2011]. Both *Hunt et al*. [2003] and *Mahoney et al*. [2011] observed increased temperatures in the upper levels of the ocean, arriving in December, peaking in January or February and then gradually decreasing in March and April. This warm water signal was also observed by moorings and conductivity-temperature-depth (CTD) measurements made under the sea ice in summer in 2005, 2006, and 2009 [*Robinson and Williams*, 2012]. *Robinson et al*. [2010] made measurements through two boreholes in the McMurdo Ice Shelf in January 2003 (marked R1 and R2 on Figure 2a). In their study, *Robinson et al*. [2010] did not observe the warm waters seen by *Hunt et al*. [2003] and *Mahoney et al*. [2011], however, it was noted that this was an anomalously cold year with heavy sea-ice conditions in McMurdo Sound, a large iceberg B-15a disturbing regular circulation patterns, and a late opening of the RSP [*Robinson et al*., 2010; *Robinson and Williams*, 2012]. *Robinson et al*. [2010] also observed barotropic diurnal tides with a maximum amplitude of ~0.2 m/s underneath the ice shelf.

3. Observations at Windless Bight

3.1. Deployment Details

[12] In November 2011, two boreholes were completed through the McMurdo Ice Shelf at Windless Bight (77°46.550′S, 167°32.400′E) and instrumented with Distributed Temperature Sensing (DTS) fiber optics, as well as traditional pressure and temperature transducers and platinum resistive thermometers. The DTS cables measured temperature in the ice shelf and ocean integrated over 1 m intervals [*Tyler et al*., 2009]. The DTS sensor had a temperature resolution of 0.03°C, and an accuracy of 0.05°C. DTS temperature measurements were made every eight times a day from November to March, and then four times a day during the winter in order to conserve electrical power. A summary of the deployment details is outlined in the

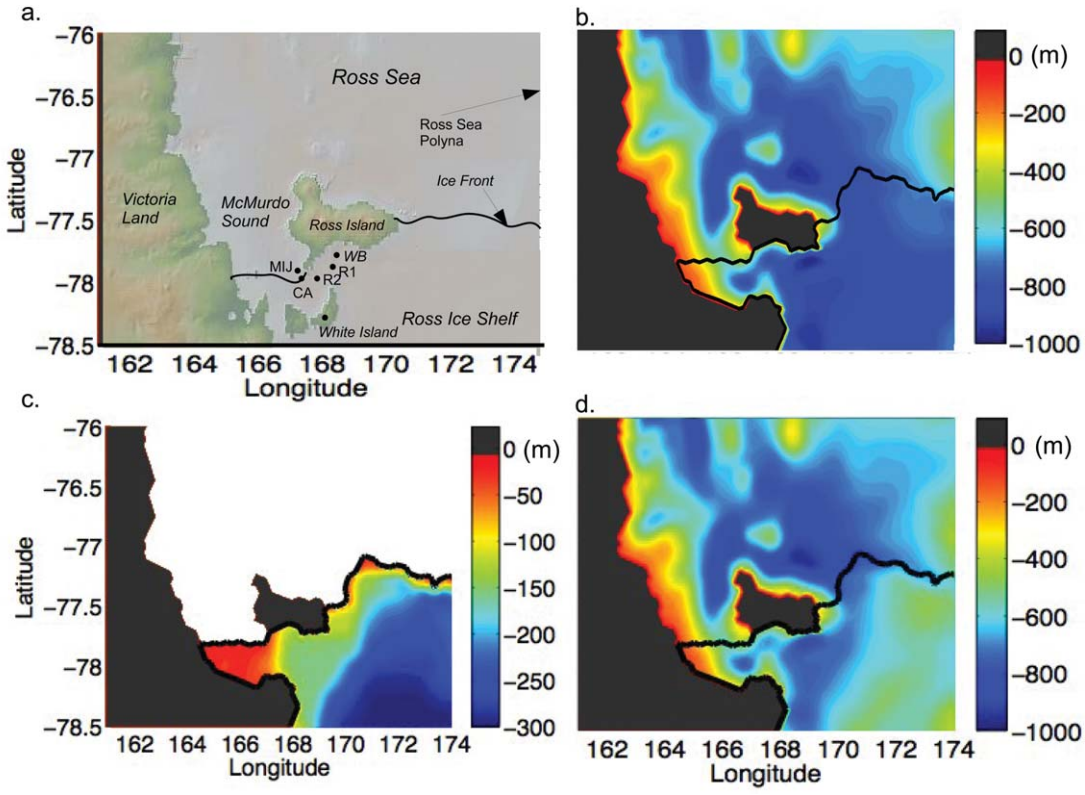

Figure 2. (a) A map of the region around McMurdo Sound. The ocean south of the black line is underneath the ice shelf. WB shows the location of Windless Bight where the boreholes in this study were drilled. R1 and R2 are the two boreholes in *Robinson et al*. [2010]. CA shows where the Cape Armitage measurements [*Mahoney et al*., 2011] were made. MIJ is the McMurdo Inlet Jetty [*Hunt et al*., 2003]. CA and MIJ are covered by multiyear sea ice near the ice front, while R1, R2, and WB are on the McMurdo Ice Shelf. (b) The bathymetry around McMurdo Sound as used in the circulation model. (c) The depth of the base of the ice shelf (below MSL). (d) The thickness of the water column. The black line in Figures 2b, 2c, and 2d represent the location of the ice front in the model [*Davey*, 2004].

supporting information. A more complete description of the deployment and calibration procedures can be found in *Tyler et al*. [2013].

3.2. Ocean Temperature Measurements

[13] The upper ice surface of the McMurdo Ice Shelf at WB is 37 m above sea level. The ice shelf thickness is 193 m, so that the ice shelf extends 156 m below sea level. The depth of the ocean below the ice surface at WB was measured as 940 ± 60 m using seismic sensors (S. Anandakrishnan, personal communication, 2011), meaning that the ocean water column thickness is 747 ± 60 m. (The model ocean thickness at WB is 697.82 m and the model ice draft is 105 m below sea level). The longest of the DTS cables deployed extended through the ice shelf and through 599 m of ocean.

[14] Figure 3a shows a detailed temporal evolution of the warm water intrusion at WB measured using the DTS system from November 2011 until June 2012. The warming of the upper water column begins in late December and continues through March. After March the temperatures start to decline to mean temperature at depth. The warmest layer (greater than $-1.6°C$) remains isolated to the upper $\sim$50 m of the water column and warm water (greater than $-1.8°C$) extends as deep as $\sim$200 m below the base of the ice shelf. At depths greater than $\sim$300 m below the base of the ice shelf, the ocean temperature remains constant $\sim -1.9°C$, which represents local surface freezing point for typical salinities. This graph represents $\sim$3 million individually recorded temperatures. The red curve in Figure 4a shows the maximum temperature recorded at WB.

3.3. Estimates Ice Shelf Melting at Windless Bight Using Observed Data

[15] In this section, we use the DTS temperature measurements to estimate the melt rate at the base of the ice shelf at WB. Since only temperature data was collected, the calculation below presents the melt rate as a rescaling of the observed temperature, and represents our best guess of the melt rates given the lack of ancillary data.

[16] The magnitude of the conductive heat flux from the ice base into the ice shelf is small compared to the turbulent heat flux from the ocean into the ice shelf base [*McPhee*, 2008]. This implies that the melt rate of the base of the ice shelf is set by the heat flux from the ocean into the ice shelf base. Since the temperature of the ice shelf base is constrained to be equal to the in situ freezing point, the heat fluxed into the ice shelf base will result in an equal latent heat flux [*Holland and Jenkins*, 1999]. This interface heat balance is described by the simplified equation

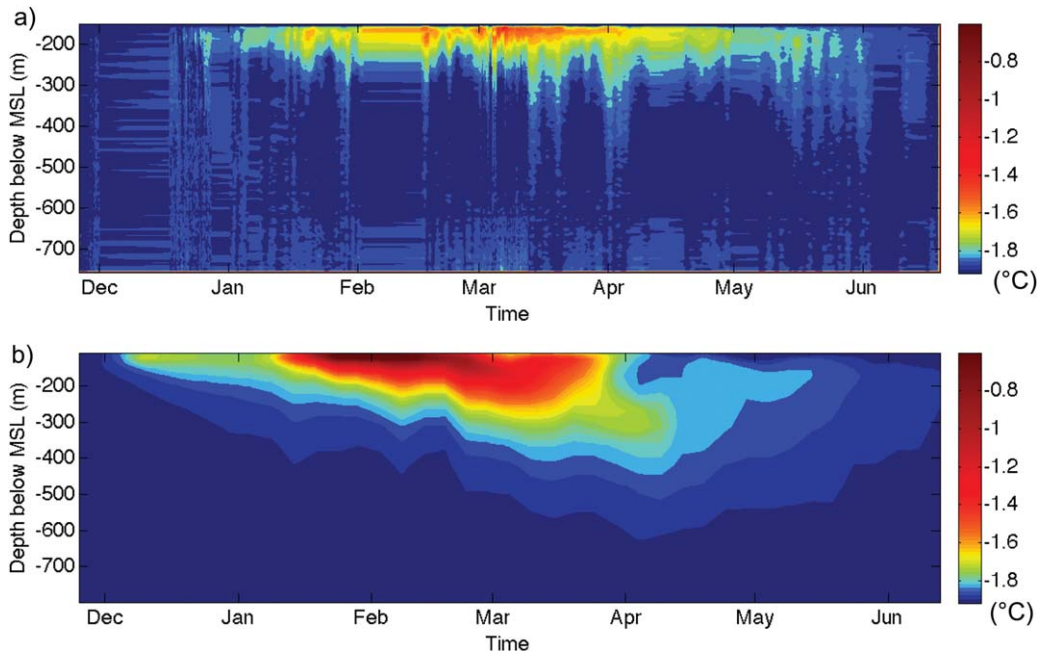

Figure 3. (a) Observations of the ocean temperature profile at Windless Bight from November 2011 to June 2012 made using a DTS fiber optic cable. Data gaps in this figure have been interpolated. (b) Model ocean temperature profile at Windless Bight from November 2010 to June 2011. The vertical axis is depth in meters below mean sea level (MSL) beginning at the base of the ice shelf. Note that the ice draft measure at Windless Bight onsite was 156 m below sea level, while the model ice draft at Windless Bight is 105 m. A significant warm water signal can be seen in the upper 200 m of the water column.

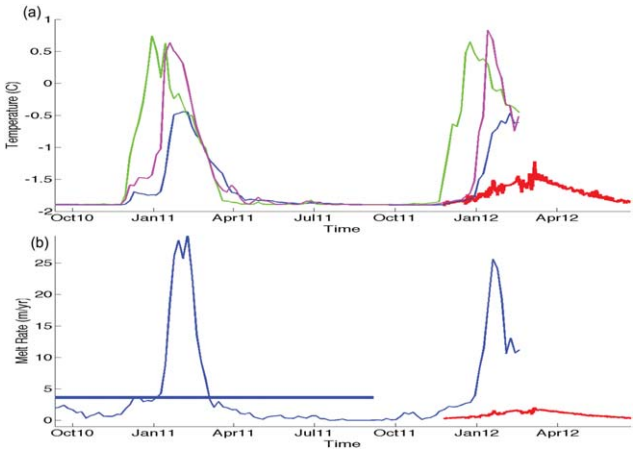

Figure 4. (a) The time evolution maximum model temperature in the water column at the selected points to the north (green) and west (magenta) of Ross Island, and also at Windless Bight (blue) to the south of Ross Island. The positions of these points are indicated in Figure 8 in the corresponding colors. The red curve in Figure 4a shows the maximum temperature observed at WB using DTS. In (b), the blue curve shows the time evolution of the model melt rate found at the grid point closest to Windless Bight. The annual mean from 15 September 2010 to 14 September 2011 is shown with a blue horizontal line. The red curve shows the melt rate estimated using observed ocean temperatures at WB.

$$<w'T'> = w_0 Q_L \tag{1}$$

[17] Here $<w'T'>$ is the turbulent heat flux from the ocean into the ice, w_0 is the vertical velocity of the ice base due to melting or freezing, and Q_L is the latent heat temperature parameter for ice [*McPhee*, 2008].

[18] Observations below sea ice suggest that turbulent heat flux of the ocean can be approximated by the formula

$$<w'T'> = St_* u_{*0}(T_w - T_f(S_w)) \tag{2}$$

[19] Here St_* is the bulk Stanton number, u_{*0} is the frictional velocity, T_w is the ocean temperature from 5 to 10 m below the ice-ocean interface, and $T_f(S_w)$ is the freezing point that the sea water at the ocean-ice interface would have if it were at the salinity of water 5 to 10 m below the ice-ocean interface [*McPhee*, 1992, 2008]. The Stanton number, formally defined by equation (2), is an empirical parameter that governs the turbulent exchange of heat though a fluid, and has been found to be approximately constant in the parameter regime considered here [*McPhee*, 1992].

[20] This bulk formula is useful in that it allows us to estimate the turbulent heat flux into the ice shelf base using only the far-field conditions. This allows us to parameterize the competing effects of turbulent mixing, which brings heat to the ice-ocean interface, and stratification near the ice-ocean interface, which suppresses heat exchange, in terms of more easily measurable variables, and allows us to estimate melt rates. This approach is widely used in numerical models where the complex small-scale behavior cannot

Table 1. Melt Rate Sensitivities Are Shown for Six Different Parameters[a]

Parameter	Parameter Value	Change in Parameter	Change in Melt Rate
Salinity	34.5 psu	0.1 psu	0.02 m/yr
Mixed layer velocity (U_M)	0.072 ms^{-1}	0.01 ms^{-1}	0.1 m/yr
Drag coefficient (c_d)	1.5×10^{-3}	0.1×10^{-3}	0.02 m/yr
Pressure (p)	156 db	10 db	0.03 m/yr
Stanton number (St_*)	0.0057	0.001	0.12 m/yr
Depth below ice shelf base	10 m	5 m	0.05 m/yr

[a]The first column shows the parameters used in the melt rate calculation. The second column shows the value of the parameters used. The third column shows the amount that the parameter is changed by in the sensitivity study. The forth column shows the change in the annual mean melt rate as a result of changing the parameter.

be resolved. The use of this bulk formulae has been well tested below sea ice [*McPhee*, 1992], and has been partially verified for use under ice shelves [*Jenkins et al*., 2010]. *Walker* [2013] showed that this approximation is reasonable provided the ice shelf base is not too steep and ocean temperatures are sufficiently close to freezing. In our case, the ice shelf base has a slope of ~0.01 [*Kovacs et al*., 1993] and the temperatures observed are less than 1° above freezing, so the errors introduced by this bulk formula are likely to be small.

[21] Following *McPhee* [2008], we assume that $w_0 = \frac{\rho_{ice}}{\rho_w}\dot{m}$. This implies

$$\frac{\rho_{ice}}{\rho_w}\dot{m}Q_L = St_* u_{*0}(T_w - T_f(S_w)) \tag{3}$$

[22] Solving for the melt rate gives

$$\dot{m} = St_* u_{*0}(T_w - T_f(S_w))\frac{\rho_w}{\rho_{ice}}(Q_L)^{-1} \tag{4}$$

[23] At WB the pressure at the base of the ice shelf is ~156 db. *Robinson et al*. [2010] measured the salinity below the McMurdo Ice Shelf to be between 34.35 and 34.72 psu. This implies an in situ sea-water freezing point of $T_f(S_w) \sim -1.99^{\circ}$C (using salinity 34.5 psu). The latent heat temperature parameter is given by $Q_L = \frac{L}{c_p}$ [*McPhee*, 2008]. Here c_p is the specific heat capacity of the ice at constant pressure, and L is the specific latent heat of melting. We use $c_p = 2093\,\frac{\mathrm{J}}{\mathrm{kgK}}$ [*Hooke*, 2005]. Since the ice at the shelf glacier base is fresh, we use $\mathrm{L} = 333.5 \times 10^3\,\frac{\mathrm{J}}{\mathrm{kg}}$. This gives $Q_L = \frac{L}{c_p} = \frac{333.5 \times 10^3 \mathrm{Jkg}^{-1}}{2093 \mathrm{Jkg}^{-1}\mathrm{K}^{-1}} = 159.3\mathrm{K}$.

[24] The frictional velocity, u_{*0} is given by $u_{*0} = \sqrt{c_d}U_m$, where c_d is the dimensionless drag coefficient, and U_m is the mixed layer velocity [*Holland and Jenkins*, 1999; *McPhee*, 2008]. We use $c_d = 1.5 \times 10^{-3}$ [*Holland and Jenkins*, 1999]. This number is subject to uncertainty since it depends on the surface roughness at the ice-ocean interface at WB, which is not known.

[25] *Robinson et al*. [2010] observed that ocean velocities beneath the ice shelf are dominated by diurnal tides. At site R2 (see Figure 2a), *Robinson et al*. [2010] observed an average velocity of 0.05 m/s to the north east, and a maximum speed of >0.15 m/s at high tide. We can get a rough estimate of the average speed under the ice shelf by adding a component due to mean currents and a component due to tides. The simplest periodic velocity function that has a mean equal to 0.05 m/s and a maximum equal to 0.15 m/s is given by $u(\theta) = 0.05 + 0.1sin(2\pi\theta))$. To get the average speed, we integrate the absolute value of this velocity over one period.

$$U_m = \int_0^1 |(0.05 + 0.1sin(2\pi\theta))|d\theta = 0.072\mathrm{m/s} \tag{5}$$

[26] This gives a frictional velocity $u_{*0} = 0.0028\mathrm{ms}^{-1}$. We use $\rho_{ice} = 920\mathrm{kg\,m}^{-3}$ and $\rho_w = 1028.4\mathrm{kg\,m}^{-3}$. Finally, we use a bulk Stanton Number $St_* = 0.0057$ [*McPhee*, 2008]. We let T_w be the ocean temperature 10 m below the ice ocean interface that we observe using DTS.

[27] Equation (4) allows us to estimate the melt rate at the base of the ice shelf at WB. This melt rate is plotted by the red curve in Figure 4b. The peak melt rate is 2.0 m/yr, and occurs on 7 March 2012. If we assume that the melt rate from the end of June to the middle of November is constant and equal to the average melt rate in June, we get an average annual melt rate is 0.71 m/yr.

[28] In the derivation above, the melt rate depends on the mixed layer velocity and salinity, which were not measured at WB, but rather taken from *Robinson et al*. [2010]. Changing the mixed layer velocity by 0.01 ms^{-1} changes the estimated annual melt rate by 0.1 m/yr. Changing the mixed layer salinity by 0.1 psu, changes the estimated annual melt rate by 0.02 m/yr. The melt rate sensitivities to other parameters are shown in Table 1. The dominant error in the above calculation comes from our lack of knowledge of the upper layer velocities.

[29] Upper layer velocities are subject to seasonal fluctuations and change with the tides. *Mahoney et al*. [2011] presented velocity data measured below the sea ice at CA. These data showed seasonal changes in the upper layer ocean velocities, which caused water to flow eastward entering the ice shelf cavity during summer and to flow northward exiting the cavity during winter. It is unclear how far under the ice shelf this current penetrates during the summer and what the current speed is by the time it reaches WB. A stronger summer current would result in an increase in the heat brought into the ice shelf cavity, and would increase the frictional velocity below the ice shelf resulting in an increased melt rate caused by the intrusion. The strong tidal velocities observed under the ice shelf by *Robinson et al*. [2010] indicate that although the accelerated summer melt rates are caused by the intrusion of warm, the melt rate impact of this warm water intrusion is significantly affected by the strength of the tidal signal.

[30] While the errors in the above estimate are large, they do give us an idea of the order of magnitude of the melt rates at WB. Comparing the red curves in Figures 4a and 4b, we see that the summer intrusion of warm water beneath the ice shelf results in seasonally accelerated summer melt rates.

[31] The uncertainties in the melt rate calculation highlight the need for ocean temperature, salinity, and velocity

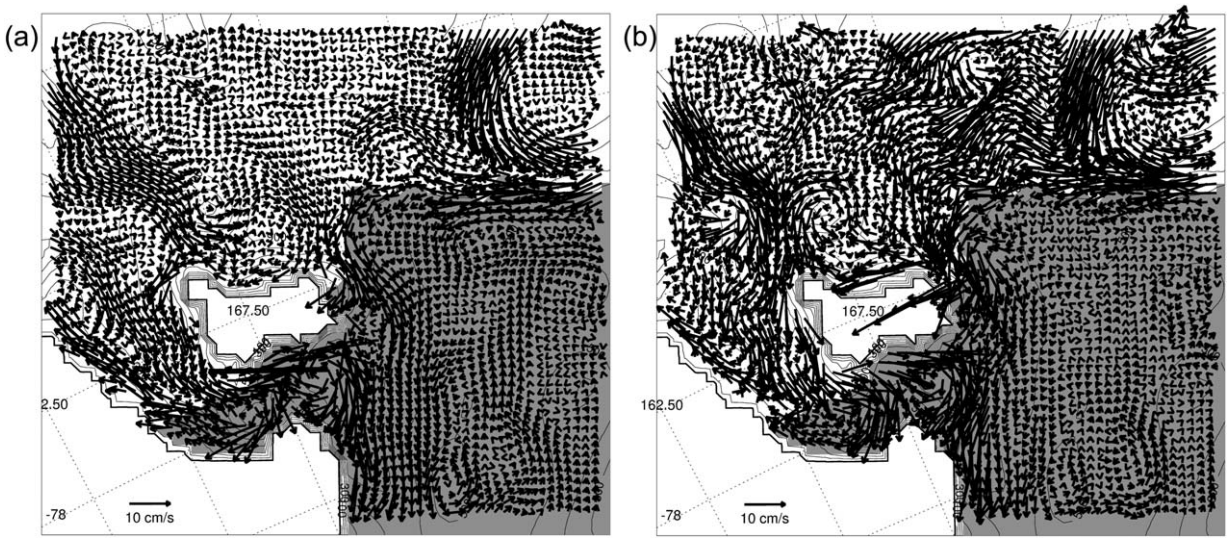

Figure 5. Mean model velocities around Ross Island. (a) The annual mean velocity at 25 m below the ocean surface (open ocean or below the ice shelf base). (b) The mean surface velocity for January 2011. The summer warm current can be seen running westward along the of Ross Island in the January profile. Shaded areas represent the location of ice shelves in the model. The thick black line near the bottom of Figure 5a indicates the position of the cross section shown in Figure 9.

profiles to be collected with independent melt rate measurements, in order to confirm the use of bulk formulae beneath ice shelves. It is especially important since these bulk formulae are commonly used to find melt rates in numerical models [*Holland and Jenkins*, 1999]. In principal, a melt rate estimate could also be derived from the ice temperature profile using inverse methods, which would provide an independent melt rate estimate.

4. Modeling of Ocean Circulation and Temperatures

4.1. Model Setup

[32] A Ross Sea model was used to simulate the ocean dynamics in and around McMurdo Sound. The aim of the simulation was to determine the source, timing, and duration of the summer warm water signal discussed above, and to determine melt rate impact of this mode 3 intrusion.

[33] The Ross Sea circulation model used is the Rutgers/UCLA Regional Ocean Modeling System (ROMS), which is a primitive equation finite difference model with a terrain following vertical coordinate system [*Haidvogel et al*., 2008; *Shchepetkin and McWilliams*, 2009]. Details of the model setup can be found in *Dinniman et al*. [2007] and *Dinniman et al*. [2011], except that the dynamic sea-ice model [*Budgell*, 2005] that was only turned on for the Bellingshausen model in *Dinniman et al*. [2011] is now active in the Ross Sea model. The dynamic sea-ice model [*Budgell*, 2005] has been added to ROMS based on ice thermodynamics described by *Mellor and Kantha* [1989] and *Hakkinen and Mellor* [1992]. The model calculates the sea-ice concentration prognostically using a two layer sea-ice representation, a snow layer and a molecular sublayer beneath the sea ice. Further details of the sea-ice model can be found in *Dinniman et al*. [2011]. Open ocean momentum, heat, and fresh water (imposed as a salt flux) fluxes for the model are calculated based on the Coupled Ocean-Atmosphere Response Experiment (COARE) 3.0 bulk flux algorithm [*Fairall et al*., 2003] and there is no relaxation of surface temperature or salinity. The model also simulates the mechanical and thermodynamic interactions between the floating Ross Ice Shelf and the water cavity underneath [*Holland and Jenkins*, 1999; *Dinniman et al*., 2011].

[34] The model domain, shown in *Dinniman et al*.'s [2011] Figure 1, includes most of the Ross Ice Shelf and Ross Sea, and extends north to 67.5°S. The horizontal grid spacing was 5 km and there were 24 vertical layers. The model topography is a combination of BEDMAP and a digitized version of an updated Ross Sea bathymetry from *Davey* [2004] (see Figure 2). For this study, a model run has been completed covering the time period 15 September 2010 to 29 February 2012. This run was forced with six hourly, 0.75° horizontal resolution, European Centre for Medium-Range Weather Forecasts (ECMWF)-Interim winds and atmospheric temperatures. The rest of the model atmospheric forcing fields (air pressure, humidity, and clouds) are the same is in *Dinniman et al*. [2007]. There are no ocean tides in this model.

4.2. Model Results

[35] Figure 5a shows the 2011 annual mean velocity field around Ross Island at 25 m below the ocean surface (open ocean or below ice shelf base). In this figure, we see water entering McMurdo Sound on the east and flowing along the western coast of Ross Island. Some of the water moves under the ice shelf, while the rest recirculates and exits McMurdo Sound along the west of the sound. The velocity field is consistent with the ocean circulation in McMurdo Sound discussed in section 2.

[36] Figure 6 shows the temperature on the level 20 model surface from December 2010 to March 2011. Since the modeling surfaces are terrain following, they have

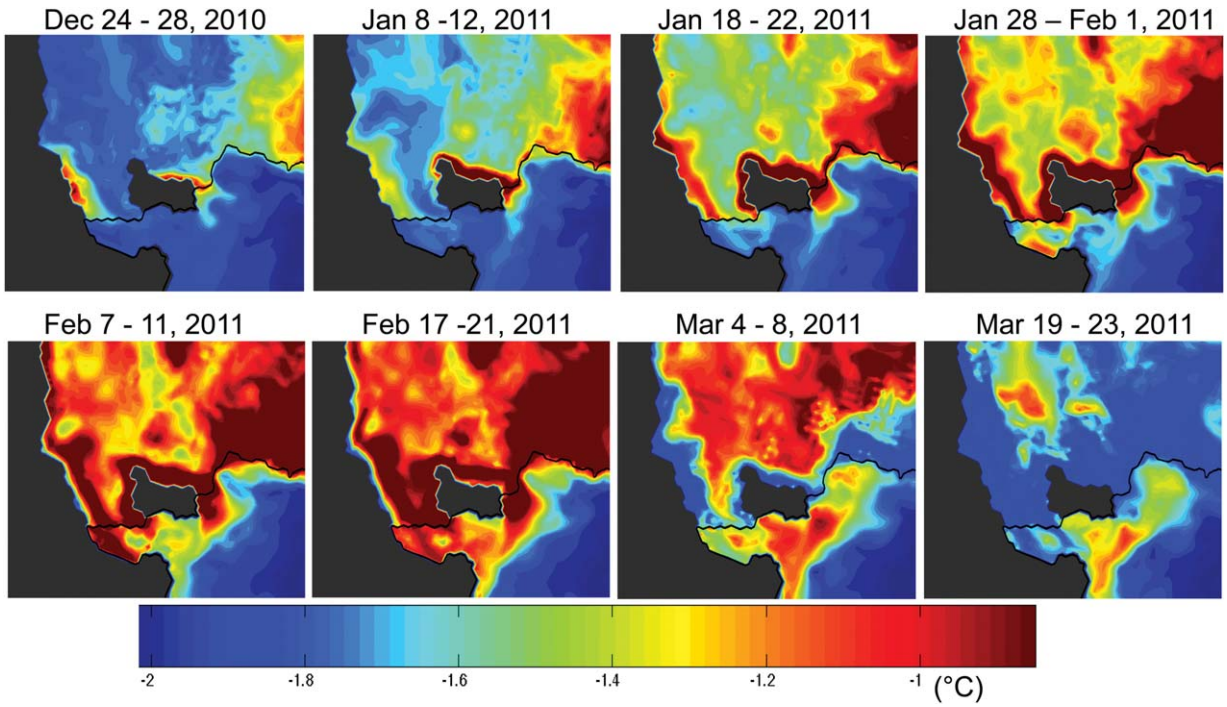

Figure 6. Ocean temperatures on the level 20 terrain following model surface from December 2010 to March 2011. The level 20 surface has a depth of around 52 m in the open ocean, and is 48 m below the ice shelf base at the grid point closest to Windless Bight. Each frame is a 5 day time average. The sequence shows the warm water signal originating to the west of the Ross Sea Polynya, being advected into McMurdo Sound and wrapping around Ross Island under the McMurdo Ice Shelf toward Windless Bight.

different depths at different points in the domain, depending on the bottom topography and ice shelf thickness. The level 20 surface has a depth of ∼52m below sea level in the open ocean around McMurdo Sound, and is ∼47m below the ice shelf base close to Ross Island, and ∼38m below the ice shelf base in the south-east Figure 6. The surface does not vary by more than 20 m below the ice shelf in the domain shown in Figure 6.

[37] In Figure 6, we see the warm water signal entering McMurdo Sound as summer arrives and disappearing as summer comes to an end. The summer signal originates to the west of the RSP in late December. CTD profiles collected in the Ross Sea confirm that water temperatures in and to the west of the RSP can be in excess of 0.5°C in the summer months [*Jacobs and Comiso*, 1989; *Saggiomo et al*., 2002]. The warm water is advected to the south-west into McMurdo Sound. It then wraps around Ross Island and moves under the McMurdo Ice Shelf toward WB. Similar summer warm water signals can be seen in all of the years simulated by the model. One other example (2003–2004 simulation) is shown in Figure S1 in the supporting information.

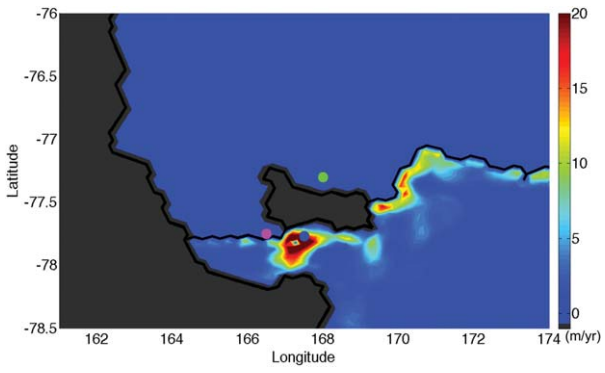

Figure 7. Melt rates at the base of the ice shelf in mid-February, at the peak of melting. The position of Windless Bight is shown with a blue dot. Selected points to the north (green) and west (magenta) of Ross Island are discussed in the text and in Figure 4.

[38] Figure 5b shows the mean surface velocity field for January 2012. In Figure 5b, one can see a strong surface current running westward from the west of the RSP, along the north of Ross Island and wrapping around Ross Island toward WB. This summertime current is strongest on the surface, and decreases in strength further down in the water column. The current is not present during the winter and is less visible in the annual mean velocity field (Figure 5a). Figure 5a also shows that there is a year round current coming from the direction of the Terra Nova Bay polynya and into McMurdo Sound. This pathway may be involved in transporting heat into McMurdo Sound later in the summer. However, Figure 6 suggests that the main source of heat at Windless Bight comes from the west of the RSP.

[39] Figure 4a shows the temporal evolution of the maximum temperature in the water column for three selected points: north of Ross Island (NR), west of Ross Island (WR) and WB. The position of these points is shown in Figure 7. In Figure 4a, we again see that the warm water

signal arrives first in the north in early December and makes its way around Ross Island, reaching WR next, and finally arriving to WB. Similarly, the temperature peak also occurs first at NR (0.74°C), then at WR (0.64°C), and finally at WB (−0.44°C).

[40] The temporal evolution of the model melt rate at WB is shown in Figure 4b. The modeled melt rate at WB peaks on 15 February 2011. Figure 7 shows the melt rates under the McMurdo (and part of the Ross) Ice Shelf for mid February 2011. In these two plots, we see that the summer warm water intrusion results in a large seasonal elevation in melt rates close to the ice front on the McMurdo Ice Shelf. The annual melt rate (15 September 2010 to 15 September 2011) at WB predicted by the model is 3.6 m/yr, but is strongly dominated by a short but strong summer melting period. Comparing Figure 7 with Figure 2c, we notice that the increased melt rates are confined to a region where the ice draft is small. Since the water intruding under the ice shelf is warm and fresh, the relatively low density of the intruding water prohibits it from penetrating deep under the ice shelf. Furthermore, as the intruding waters travel deeper under the ice shelf, the density is decreased by interaction with melt water from the base of the ice shelf. The large ice shelf draft essentially creates a shadow zone where the intruding surface waters can not penetrate.

[41] Figure 8 shows the trajectory of four sets of 3-D model Lagrangian floats released to the north east of Ross Island, in the location of the RSP. Each group of floats consists of 10 floats that were allowed to drift for 120 days. Figures 8a, 8b, and 8c show floats that were released on the level 20 model surface on 1 December 2011, 16 December 2011, and 31 December 2011, respectively. Figure 8d shows the trajectory of floats released at the surface on 16 December 2011.

[42] The floats released on 1 December 2011 (Figure 8a) do not appear to have a preferred drift direction. A few of the floats drift toward Ross Island making their way beneath the ice shelf to the east of Ross Island. One of the floats moves westward and makes its way into McMurdo Sound. Once this float is in McMurdo Sound, it wraps around the west of Ross Island and moves in the direction of WB. The floats released on December 16th (Figure 8b) appear to move in a more organized way. All of the floats either move to the north east, or else move south west toward Ross Island. Some of these floats wrap around the east and west of Ross Island and move under the ice shelf. The floats released on 31 December 2011 move in a similar fashion except that a greater number of floats move westward along the north of Ross Island, wrap around the west of Ross Island, and move under the ice shelf toward WB. Figure 8d shows that for floats released at the surface on December 16th, an even greater number of floats follow the pathway from the RSP, around Ross Island, and under the ice shelf toward WB. Some of the floats exit the ice shelf cavity on the west of McMurdo Sound and follow the western coastline out of McMurdo Sound. A few of the deeper floats move past WB and move deeper under the ice shelf.

[43] The float trajectories indicate that there is a summer current that moves water from the west of the RSP around the north of Ross Island and into McMurdo Sound. This current appears to be surface intensified and results in water closer to the surface being more strongly steered along this pathway. The current appears to strengthen as summer advances. This summer current is also seen in model summer mean surface velocity fields (not shown). These model results suggests that the summer warm water signal observed at WB, or at least part of it, is likely to have originated to the west of the RSP, and have followed the same path as the drifters toward WB.

[44] The onset of the westward current leading from the RSP to McMurdo Sound is most likely caused by the melting of the sea ice in the west of the RSP. As the sea ice melts, the surface water closer to the coast becomes warmer, fresher and less dense than the water beneath the sea ice further to the north. This density difference drives a westward current, which moves water from the RSP to McMurdo Sound. The fresh surface water is decoupled from the bathymetry below, and this allows a surface intensified current to form. This generation mechanism is consistent with the model data. This mechanism is analogous to the mechanism driving a seasonal coastal current along the Antarctic Peninsula that was found by *Moffat et al*. [2008].

[45] Cross sections of the salinity, potential temperature, and potential density across the ice front for late January 2011 are shown in Figures 9a, 9b, and 9c, respectively. A cross section of the potential temperature across the ice front for late February is shown in Figure 9d. Winter salinity and potential temperature sections from late September are shown in Figures 9e and 9f. All sections in Figure 9 are 5 day averages beginning on the dates indicated.

[46] Figure 9 shows that the warm water moving toward WB subducts as it moves under the shelf, rather than entering the ice shelf cavity through horizontal advection (which would produce horizontal temperature contours). This implies that the intrusion is a mode 3 rather than a mode 2 intrusion. Further east on the Ross Ice Shelf, Modified Circumpolar Deep Water (MCDW) is able to move under the ice shelf at a depth of 200–400 m [*Dinniman et al*., 2011; *Orsi and Wiederwohl*, 2009]. This appears not to happen in McMurdo Sound. Figure 9 also shows that as the water subducts under the ice shelf, it cools as it travels along the ice shelf base. The heat is transmitted into the ice shelf causing melting. By late February the water at the ice shelf base is cooler than the water directly below it (Figure 9d). In winter, the warm water signal disappears entirely and the water column becomes almost homogenous (Figures 9e and 9f).

[47] The structure of the surface intensified warm water signal indicates that a large portion of the heat entering McMurdo Sound must come from solar insolation. This result is consistent with *Robinson and Williams* [2012] who used CTD and mooring data to show that the warm water entering McMurdo Sound in summer was Antarctic Surface Water. Figure 8 shows that the intruding warm waters originate in the south west of the RSP. Observations of ocean temperature profiles in the region in the south west of the RSP show that once the sea ice has cleared, the sun is able to heat the top of the water column, creating a temperature maximum at the top of the water column [*Jacobs and Comiso*, 1989; *Reddy et al*., 2010]. The warming of the surface waters in the south west of the RSP could not have occurred without the region becoming ice free because this

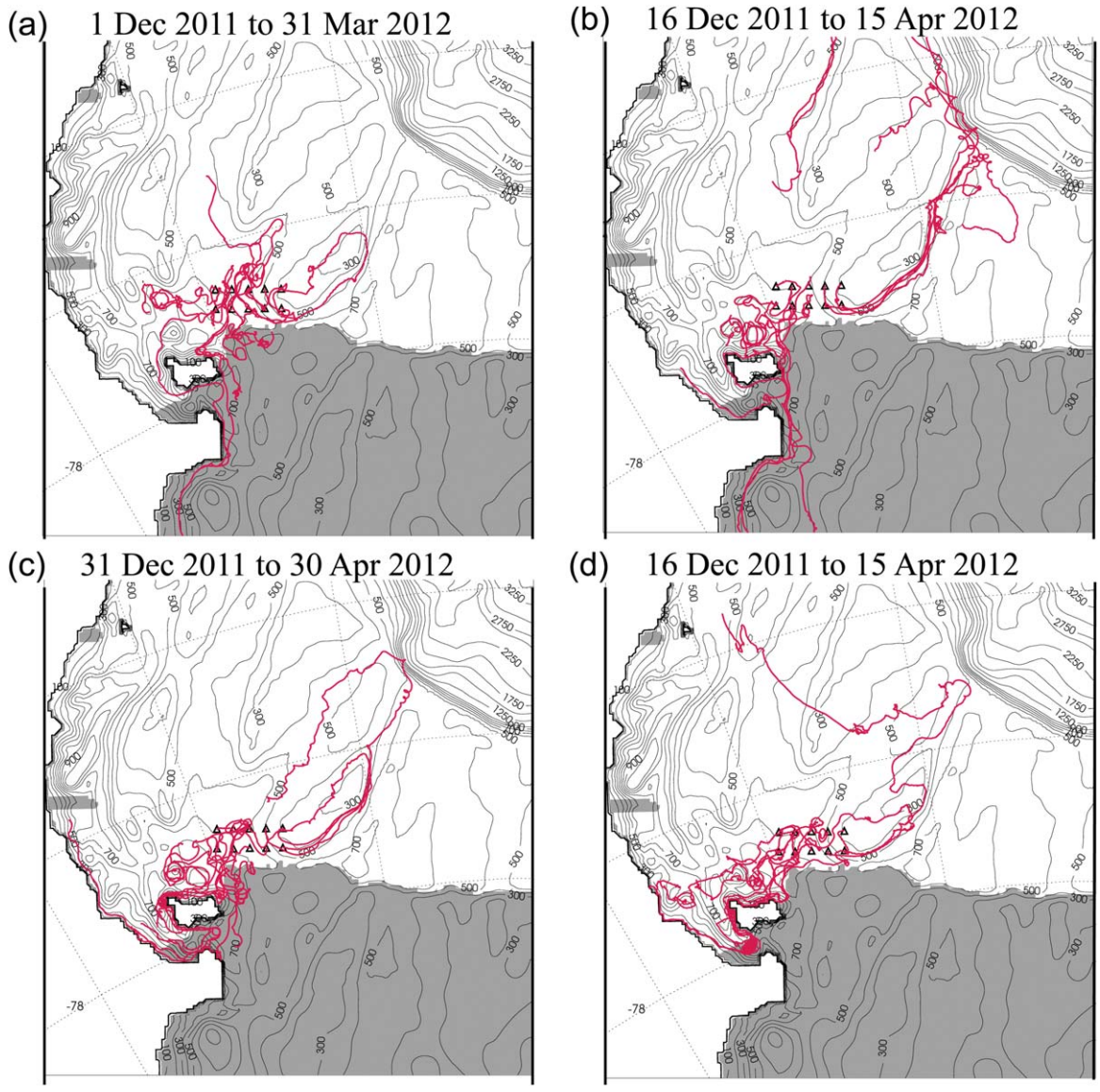

Figure 8. The trajectories of four groups of 3-D Lagrangian model floats are shown. Each group of floats consists of 10 floats which were allowed to drift for 120 days. The initial position of the floats is indicated by the black triangles. Floats released at model level 20 on (a) 1 December 2011, (b) 16 December 2011, and (c) 31 December 2011. (d) Floats released at the surface on 16 December 2011.

would require another source of heat. While some heat contribution might come from MCDW [*Jacobs and Comiso*, 1989; *Reddy et al*., 2010], most of the MCDW heat is lost when the it mixes to the surface during the fall/winter. The temperature maximum at the surface could not have been created by upwelling of MCDW alone since this would create a temperature maximum lower down in the water column.

[48] Since the source of the heat for the warm water intrusion is through solar insulation in the south west of the RSP, the arrival of the warm water intrusion can not occur until the RSP becomes ice free. The time of this arrival varies slightly from year to year because of interannual variability in the sea-ice conditions [*Martin et al*., 2007; *Robinson and Williams*, 2012]. One example of this was in 2003, when the presence of large icebergs resulted in a late opening of the RSP, which had a significant effect on the temperatures measured in McMurdo Sound [*Robinson and Williams*, 2012].

[49] Figure 3b shows how the ocean profile at WB in the model varies with time. In this figure we see the annual arrival of warm water and the vertical structure of this warm water signal.

4.3. Model Sea-Ice Conditions

[50] The above results imply that the timing of the warm water intrusion depends on the timing of the opening of the RSP. It is therefore important that our model should be able to correctly simulate the sea-ice conditions over the Ross Sea if we hope for the timing of the model intrusion to match the observed intrusion. Recall that our model includes a dynamic sea-ice model [*Budgell*, 2005].

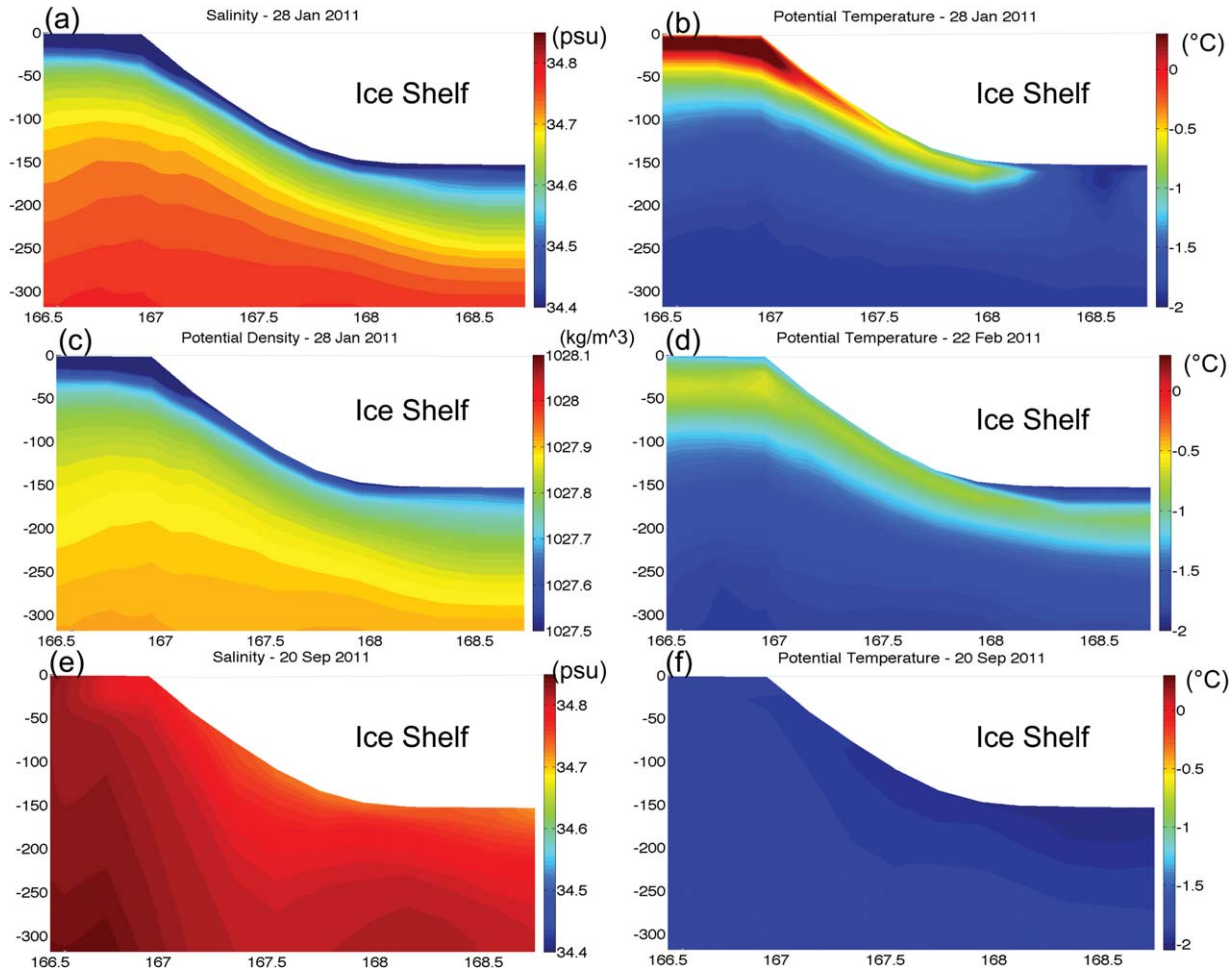

Figure 9. Cross sections of model results running across the ice shelf front in the south of McMurdo Sound in 2011. The position of these cross sections is shown in Figure 5a. (a) The salinity in late January 2011. (b) The potential temperature in late January 2011. (c) The potential density in late January 2011. (d) The potential temperature in late February 2011. (e) The salinity in late September 2011. (f) The potential temperature in late September 2011. The warm near-surface water at the ice front subducts under the ice shelf. The water then cools as it moves along the ice shelf base. In winter, the water column becomes homogenous. The McMurdo Ice Front is 20 m high, which is why it appears to be so smooth [*Kovacs et al*., 1993; *Robinson et al*., 2010].

[51] The model sea-ice results compare well to sea-ice satellite observations. The integrated sea-ice area over the entire domain and over the continental shelf is used to quantify the comparison between the model results and the Special Sensor Microwave Imager/Sounder (SSMIS) sea-ice satellite observations [*Maslanik and Stroeve*, 1999]. The model output and satellite observations have a correlation of $r = 0.956$ over the entire model domain and $r = 0.946$ over the continental shelf. This high correlation indicates that the model does a good job of representing the timing of seasonal changes in the ice concentration and the opening of the RSP.

[52] Figure 10 shows how the integrated sea-ice area over the entire domain and over the continental shelf varies with time. The model is slow to first open up the polynya compared with SSMIS, and has a consistent lag during the period when the sea-ice area is decreasing. The model does a good job simulating the timing and area of the summertime sea-ice minimum across the entire domain and on the continental shelf. The timing of the ice coming back in the fall is also well reproduced. The model has too much sea ice at the time of maximum sea-ice extent. The spatial structure of the RSP (not shown) also compares well with observations.

5. Discussion

5.1. Comparing Observations with Model Results

[53] The maximum ocean temperature recorded at WB occurred on 7 March 2012 and was −1.19°C. This is considerably cooler than the temperature maximum observed in previous campaigns by moorings under the sea ice (−0.08°C at CA in late January 2008 [*Mahoney et al*., 2011]; −0.43°C in mid January 2000 and −0.65°C in early February 2001 at MIJ [*Hunt et al*., 2003]). This is consistent with the model results that showed subduction and cooling of the warm water as it moved under the ice shelf (Figure 4). The temperature maximum also arrives

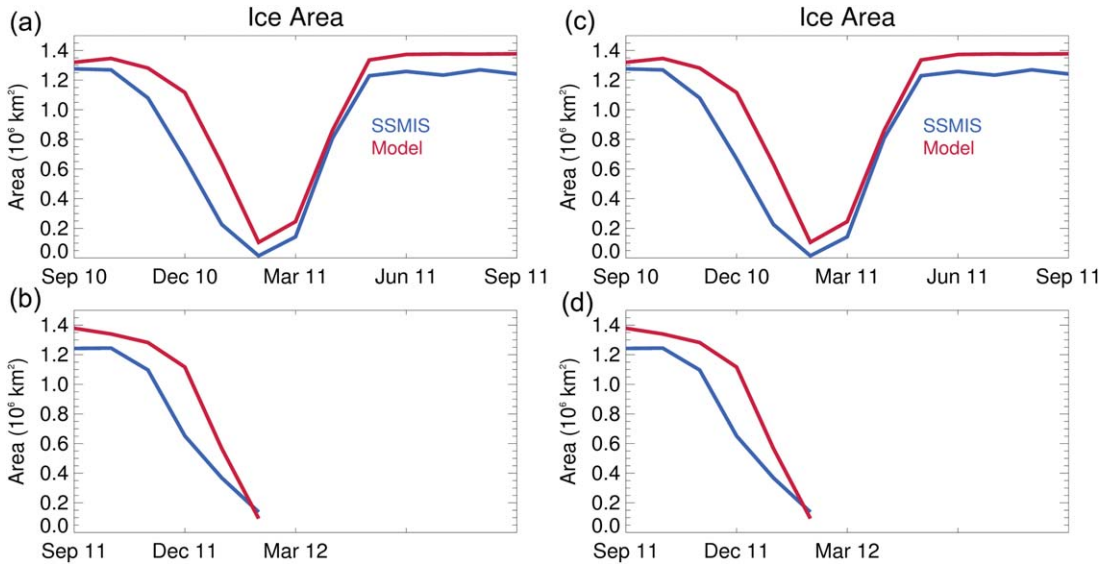

Figure 10. Integrated sea-ice cover over the (a and b) Ross Sea and (c and d) Ross Sea continental shelf. Model results are shown in red and SSMIS satellite observations are shown in blue.

substantially later at WB than it had under the sea ice in any of measurements from previous years. The maximum modeled ocean temperature recorded at WB in 2011 occurred on 25 February 2011.

[54] The modeling results and the newly acquired observations provide further evidence that the warm water summer signal seen below the sea ice by *Mahoney et al*. [2011] and *Hunt et al*. [2003] at CA is a regular annual signal, and that it is advected from northeast of Ross Island into McMurdo Sound. Furthermore, the results confirm that the warm water signal does manage to propagate below the McMurdo Ice Shelf and eventually arrives at WB, where it causes elevated melt rates during the summer.

[55] Comparing the modeled temperature profile at WB (Figure 3b) to the observed temperature profile at WB (Figure 3a), we see that the model captures many of the features seen in the observational data. Both the model and observations at WB show the arrival of the summer warm water signal in January. The initial warm water signal occurs in the upper portion of the water column close to the base of the ice shelf. During February the intrusion becomes stronger and extends deeper in the water column. The highest temperatures are found at the top of the water column, close to the base of the ice shelf. The summer signal peaks at the end of summer, with maximum temperatures occurring in late February (model) and early March (observations). In the fall, the temperatures decrease and by June, the water column is almost isothermal. During the fall there is a temperature inversion in the water column in both the model and observations. The ocean temperatures just below the ice shelf cool fastest, which results in the water column having cooler water temperatures at the top of the water column and warmer temperatures just below. The lower portion of the water column is largely unaffected by the warm water intrusion, and remains at $\sim -1.9°C$ throughout the observed period. The warm water signal observed at WB is cooler than the signal predicted by the model. The observed signal persists longer than the modeled warm water signal and is confined more tightly to the upper layer. The model warm water signal from 2011 arrives two weeks earlier than the signal in the observations from 2012.

[56] The model predicted an annual average melt rate of 3.6 m/yr at WB, which was higher than the annual average melt rate estimated from the observed ocean temperatures (0.71 m/yr). One reason for this was that the modeled temperature of the warm water intrusion at WB was up to $\sim 1°C$ warmer than the observed temperatures. Examining the modeled melt rate data more carefully (Figure 8), we notice that WB is in a region that has a steep gradient in the melt rates since it is right on the edge of a high melting zone. The three model points immediately to the east of WB have annual melt rates of 2.9, 1.5, and 0.6 m/yr. These large spatial gradients in the melt rate are a result of similar large spatial gradients in the bathymetry data around WB (since the warmest water is steered by the bathymetry). The resolution and accuracy of the bathymetry data used in the model is another likely source of error in determining the ultimate melt rates.

[57] The fact that the model is able to reproduce the summer water intrusion under McMurdo Ice Shelf without including the complex topography around Ross Island and without including tides, indicates that the local oceanography under the McMurdo Ice Shelf is strongly controlled by the larger circulation in the Ross Sea. The calculation for the melt rate estimate shown in section 3.3 indicates that tidal currents may be significant for determining the basal melting caused by this intrusion.

[58] The annual melt rate is heavily dominated by a short period of extreme melting. This implies that attempting to predict this melt rate using a model will be sensitive to the strength and duration of the warming period. Since these both depend on sea-ice conditions further north, it is likely to be a difficult problem, and a source of inaccuracy for coupled models that do not use prescribed sea-ice concentrations. This difficulty is likely to be common to most mode 3 warm water intrusions.

[59] The modeling results shown above indicate that the RSP is the source of the warm water signal observed beneath the McMurdo Ice Shelf. This result suggests that mode three intrusions may be associated with the opening of the polynyas in other regions in Antarctica. *Hattermann et al*. [2012] observed a mode 3 intrusion of warm water near the ice front beneath the Fimbul Ice Shelf. This intrusion occurred in late summer and was associated with the ocean near the ice front becoming ice free [*Hattermann et al*., 2012]. Further observations and modeling efforts are needed to determine whether there are further examples of this phenomenon.

6. Conclusion

[60] High resolution, semiannual ocean temperature profiles measured at WB on the McMurdo Ice Shelf from November 2011 to June 2012 reveal a warm water summer signal that penetrates under the McMurdo Ice Shelf and results in increased melting. A regional Ross Sea ocean model is used to simulate the mode 3 summer intrusion. Model results are compared with observations of temperatures below the sea ice and ice shelf south of Ross Island. The results presented above shed light on the source, timing, and melt rate impact of the warm water intrusion.

[61] The model shows that the warm water signal seen at WB originates in the region to the north-east of Ross Island, west of the Ross Sea Polynya. Once the sea ice in this region has cleared, the Sun heats the ocean surface, which causes warming in the upper part of the ocean. The warm water is transported into McMurdo Sound by ocean currents, where some of the water subducts under the ice shelf and is able to wrap around Ross Island toward Windless Bight. As the intruding water moves along the ice shelf base, it is cooled due to glacier ice melting, eventually resulting in a temperature inversion. The warm water under the ice shelf results in seasonally accelerated melt rates. The extent of the melt rate impact is strongly controlled by bathymetry.

[62] The model was able to simulate the structure of the temporal evolution of the ocean temperature profile at Windless Bight. The maximum model temperatures achieved were $\sim$1°C higher than those observed, resulting in a melt rate that was higher than the melt rate inferred from ocean temperature observations. This highlights the sensitivity of the melt rates caused by mode 3 intrusions to the strength and duration of the intrusion and also to the accuracy of bathymetry data used. The elevated melt rates occurring for short periods of time, implies that predicting the total contribution of mode 3 intrusions on the melt rates of Antarctic ice shelves is likely to present a challenge to numerical models.

[63] This study presents one of the first successful incorporations of high spatial and temporal resolution data from fiber optic sensing in an ice shelf, which could be an exciting new measurement technique for Polar Regions. The above findings provides motivation for the establishment of a wide network of ice shelf monitoring stations which can be used to constrain and validate numerical models on a larger scale.

[64] **Acknowledgments.** Funding for this project has been provided by the Office of Polar Programs of the U.S. National Science Foundation (NSF) under grants ANT-1043395 (NYU), ANT-1043217 (OSU), and ANT-10431154 (UNR). Support for D. M. Holland was provided by Abu Dhabi grant G1204. Support for M. S. Dinniman was provided by the U.S. NSF (ANT-0838948 and ANT-0944174). Additional instrument support was provided by NSF-CTEMPs under EAR-1128999, and engineering services were provided by the UNAVCO facility with support from the NSF and NASA under NSF Cooperative Agreement EAR-0735156. Thanks to S. Kobs who helped with calibration of the DTS data. We would also like to acknowledge the contribution of two anonymous reviewers for their thoughtful criticisms and suggestions for improvements to this paper.

References

Bindschadler, R., D. G. Vaughan, and P. Vornberger (2011), Variability of basal melt beneath the Pine Island Glacier ice shelf, West Antarctica, *J. Glaciol.*, *57*(204), 581–595.

Budgell, W. P. (2005), Numerical simulation of ice-ocean variability in the Barents Sea region: Towards dynamical downscaling, *Ocean Dyn.*, *55*(3–4), 370–387.

Davey, F. J. (2004), Ross Sea Bathymetry, in *Institute of Geological & Nuclear Sciences Geophysical Map 16*, scale 1:2,000,000, Version 1.0., Inst. of Geol. & Nucl. Sci., Lower Hutt, N. Z.

Dinniman, M. S., J. M. Klinck, and W. O. Smith Jr. (2007), The influence of sea ice cover and icebergs on circulation and water mass formation in a numerical circulation model of the Ross Sea, Antarctica, *J. Geophys. Res.*, *112*, C11013, doi:10.1029/2006JC004036.

Dinniman, M. S., J. M. Klinck, and W. O. Smith Jr. (2011), A model study of circumpolar deep water on the West Antarctic Peninsula and Ross Sea continental shelves, *Deep Sea Res., Part II*, *58*, 1508–1523, doi:10.1016/j.dsr2.2010.11.013.

Dinniman, M. S., J. M. Klinck, and E. E. Hofmann (2012), Sensitivity of circumpolar deep water transport and ice shelf basal melt along the West Antarctic Peninsula to changes in the winds, *J. Clim.*, *58*, 4799–4816, doi:10.1175/JCLI-D-11–00307.1.

Fairall, C. W., E. F. Bradley, J. E. Hare, A. A. Grachev, and J. B. Edson (2003), Bulk parameterization of airsea fluxes: Updates and verification for the COARE algorithm, *J. Clim.*, *16*, 571–591.

Haidvogel, D. B., et al. (2008), Ocean forecasting in terrain following coordinates: Formulation and skill assessment of the RegionalOceanModeling System, *J. Comput. Phys.*, *227*, 3595–3624, doi:10.1016/j.jcp.2007.06.016.

Hakkinen, S., and G. L. Mellor (1992), Modeling the seasonal variability of a coupled arctic ice-ocean system, *J. Geophys. Res.*, *97*, 20,285–20,304.

Hattermann, T., O. A. Nost, J. M. Lilly, and L. H. Smedsrud (2012), Two years of oceanic observations below the Fimbul Ice Shelf, Antarctica, *Geophys. Res. Lett.*, *39*, L12605, doi:10.1029/2012GL051012.

Holland, D. M., and A. Jenkins (1999), Modeling thermodynamic ice-ocean interactions at the base of an ice shelf, *J. Phys. Oceanogr.*, *29*, 1787–1800.

Holland, D. M., S. S. Jacobs, and A. Jenkins (2003), Modeling Ross Sea ice shelf—Ocean interaction, *Antarct. Sci.*, *15*, 13–23.

Hooke, R. L. (2005), *Principles of Glacier Mechanics*, 2nd ed., 14 pp., Cambridge Univ. Press, U. K.

Horgan, H. J., R. T. Walker, S. Anandakrishnan, and R. B. Alley (2011), Surface elevation changes at the front of the Ross Ice Shelf: Implications for basal melting, *J. Geophys. Res.*, *116*, C02005, doi:10.1029/2010JC006192.

Hunt, B. M., K. Hoefling, and C. C. Cheng (2003), Annual warming episodes in seawater temperatures in McMurdo Sound in relationship to endogenous ice in notothenioid fish, *Antarct. Sci.*, *15*, 333–338 doi:10.1017/S0954102003001342.

Jacobs, S. S., and J. C. Comiso (1989), Sea ice and oceanic processes on the Ross Sea continental-shelf, *J. Geophys. Res.*, *94*, 18,195–18,211.

Jacobs, S. S., H. H. Helmer, C. S. M. Doake, A. Jenkins, and R. M. Frolich (1992), Melting of ice shelves and the mass balance of Antarctica, *J. Glaciol.*, *38*(130), 375–387.

Jacobs, S. S., A. Jenkins, C. F. Giulivi, and P. Dutrieux (2011), Stronger ocean circulation and increased melting under Pine Island Glacier ice shelf, *Nat. Geosci.*, *4*, 519–523, doi:10.1038/ngeo1188.

Jenkins, A., K. W. Nicholls, and H. F. Corr (2010), Observation and parameterization of ablation at the base of Ronne Ice Shelf, Antarctica, *J. Phys. Oceanogr.*, *40*(10), 2298–2312.

Kovacs, A., A. J. Gow, and R. M. Morey (1993), A reassessment of the in-situ dielectric constant of Polar Firn, *Cold Regions Research & Engineering Laboratory Report 93-26.*

Leonard, G. H., C. R. Purdie, P. J. Langhorne, T. G. Haskell, M. J. M. Williams, and R. D. Frew (2006), Observations of platelet ice growth and oceanographic conditions during the winter of 2003 in McMurdo Sound, Antarctica, *J. Geophys. Res.*, *111*, C04012, doi:10.1029/2005JC002952.

Lewis, E. L., and R. G. Perkin (1985), The winter oceanography of McMurdo Sound, Antarctica, *Antarct. Res. Ser.*, *43*, 145–166.

Littlepage, J. L. (1965), Oceanographic investigations in McMurdo Sound, Antarctica, *Antarct. Res. Ser.*, *5*, 1–37.

MacAyeal, D. R. (1984), Thermohaline circulation below the Ross Ice Shelf: A consequence of tidally induced vertical mixing and basal melting, *J. Geophys. Res.*, *89*, 597–606, doi:10.1029/JC089iC01p00597.

Mahoney, A. R., A. J. Gough, P. J. Langhorne, N. J. Robinson, C. L. Stevens, M. M. J. Williams, and T. G. Haskell (2011), The seasonal appearance of ice shelf water in coastal Antarctica and its effect on sea ice growth, *J. Geophys. Res.*, *116*, C11032, doi:10.1029/2011JC007060.

Makinson, K., M. Schrder, and S. sterhus (2006), Effect of critical latitude and seasonal stratification on tidal current profiles along Ronne Ice Front, Antarctica, *J. Geophys. Res.*, *111*, C03022, doi:10.1029/2005JC003062.

Martin, S., R. Drucker, and R. Kwok (2007), The areas and ice production of the western and central Ross Sea polynyas, 19912002, and their relation to the B-15 and C-19 iceberg events of 2000 and 2002, *J. Maine Syst.*, *68*, 201–214, doi: 10.1016/j.jmarsys.2006.11.008.

Maslanik, J., and J. Stroeve (1999), Near-Real-Time DMSP SSM/I-SSMIS Daily Polar Gridded Sea Ice Concentrations, 15 Sep. 2010 to 29 Feb. 2012, Natl. Snow Ice Data Cent., Digital Media, Boulder, Colo.

McPhee, M. (2008), *Air-Ice-Ocean Interactions: Turbulent Ocean Boundary Layer Exchange Processes*, chap. 6, pp. 109–131, Springer, N. Y.

McPhee, M. G. (1992), Turbulent heat flux in the upper ocean under sea ice, *J. Geophys. Res.*, *97*, 5365–5379.

Mellor, G. L., and L. Kantha (1989), An ice-ocean coupled model, *J. Geophys. Res.*, *94*, 10,937–10,954.

Mitchell, W. M., and J. A. T. Bye (1985), Observations in the boundary layer under the sea ice in McMurdo Sound, in *Oceanology of the Antarctic Continental Shelf, Antarct. Res. Ser*., vol. *43*, edited by S. Jacobs, pp. 167–176, AGU, Washington, D. C., doi:10.1029/AR043p0167.

Moffat, C., R. C. Beardsley, B. Owens, and N. van Lipzig (2008), A first description of the Antarctic Peninsula Coastal Current, *Deep Sea Res., Part II*, *55*(3–4), 277–293.

Nicholls, K. W. (1996), Temperature variability beneath Ronne Ice Shelf, Antarctica, from thermistor cables, *J. Phys. Oceanogr.*, *11*, 1199–1210.

Orsi, A. H., and C. L. Wiederwohl (2009), A recount of Ross Sea water, *Deep Sea Res., Part II*, *56*, 778–795.

Pritchard, H. D., S. R. M. Ligtenberg, H. A. Fricker, D. G. Vaughan, M. R. van den Broeke, and L. Padman (2012), Antarctic ice-sheet loss driven by basal melting of ice shelves, *Nature*, *484*, 502–505, doi:10.1038/nature10968.

Reddy, T., D. M. Holland, and K. Arrigo (2010), Ross ice shelf cavity circulation, residence time, and melting: Results from a model of oceanic chlorofluorocarbons, *Cont. Shelf Res.*, *30*(7), 733–742.

Robinson, N. J., and M. J. M. Williams (2012), Iceberg-induced changes to polynya operation and regional oceanography in the southern Ross Sea, Antarctica, from in situ observations, *Antarct. Sci.*, *24*, 514–526.

Robinson, N. J., M. J. M. Williams, P. J. Barrett, and A. R. Pyne (2010), Observations of flow and ice-ocean interaction beneath the McMurdo Ice Shelf, Antarctica, *J. Geophys. Res.*, *115*, C03025, doi:10.1029/2008JC005255.

Saggiomo, V., G. Catalano, O. Mangoni, G. Budillon, and G. C. Carrada (2002), Primary production processes in ice-free waters of the Ross Sea (Antarctica) during the austral summer 1996, *Deep Sea Res., Part II*, *49*, 1787–1801.

Shchepetkin, A. F., and J. C. McWilliams (2009), Correction and commentary for ''Ocean forecasting in terrain-following coordinate: Formulation and skill assessment of the regional ocean modeling system'' by Haidvogel et al., *J.Comput. Phys.*, *227*, 3595–3634, J. Comput. Phys., 228, 8985–9000, doi:10.1016/j.jcp.2009.09.002.

Tyler, S. W., J. S. Selker, M. B. Hausner, C. E. Hatch, T. Torgersen, C. E. Thodal, and S. G. Schladow (2009), Environmental temperature sensing using Raman spectra DTS fiber-optic methods, *Water Resour. Res.*, *45*, W00D23, doi:10.1029/2008WR007052.

Tyler, S. W., D.M. Holland, V. Zagorodnov, A. A. Stern, C. Sladek, S. Kobs, S. White, F. Suarez, and J. Bryenton (2013), Instruments and methods using distributed temperature sensors to monitor an Antarctic ice shelf and sub-ice-shelf cavity, *J. Glaciol.*, *59*(215), 583–591, doi:10.3189/2013JoG12J207.

Walker, R. T., D. M. Holland, B. R. Parizek, R. B. Alley, S. M. J. Nowicki, and A. Jenkins (2013), Efficient flowline simulations of ice-shelf/ocean interactions: Sensitivity studies with a fully coupled model, *J. Phys. Oceanogr.*, *43*, 2200–2210.